View Article Online
View Journal

Dalton
Transactions

Accepted Manuscript

This article can be cited before page numbers have been issued, to do this please use: J. Balbuena, J. M. Calatayud, M. Cruz, P. Pardo, F. Martín, J. Alarcón and L. Sanchez, *Dalton Trans.*, 2018, DOI: 10.1039/C8DT00721G.

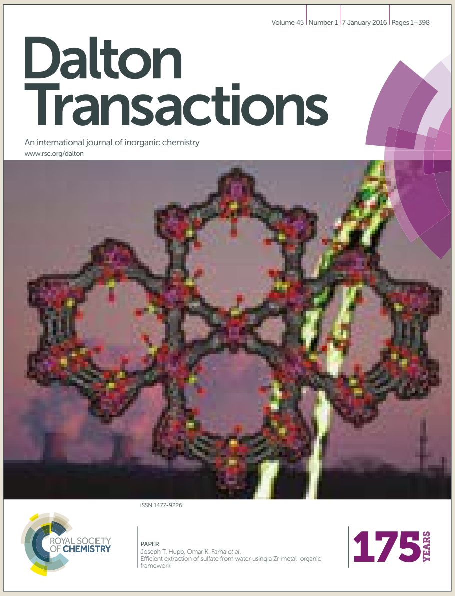

ROYAL SOCIETY
OF CHEMISTRY

rsc.li/dalton

View Article Online
DOI: 10.1039/C8DT00721G

Dalton Transactions

ARTICLE

Mesocrystalline anatase nanoparticles synthesized by a simple hydrothermal approach with enhanced light harvesting for gas-phase reaction

Received 00th January 20xx,
Accepted 00th January 20xx

DOI: 10.1039/x0xx00000x

www.rsc.org/

José Balbuena,[a] José Miguel Calatayud,[b] Manuel Cruz-Yusta,[a] Pablo Pardo, [b] Francisco Martín, [c] Javier Alarcón,*[b] and Luis Sánchez*[a]

Mesocrystalline TiO_2 nanoparticles are synthesized by a hydrothermal approach. A simple two-step procedure at low temperature (< 140 °C) let the nucleation of primary particles sized 2-4 nm and their subsequent assembly as almost spherical aggregates sized ≈ 20 nm. X-ray powder diffraction (XRD), Raman and X-ray photoelectron (XPS) spectroscopies, and HRTEM studies confirm the anatase as unique TiO_2 crystalline phase. The mesocrystalline structure of the anatase aggregates is clearly evidenced by HRTEM and SAED. The mesocrystalline nanopowders exhibit a mesopore structure with surface area and pore volume of 63.5 $m^2 \cdot g^{-1}$ and 0.22 $cm^3 \cdot g^{-1}$, respectively. Apart from ultraviolet (UV), visible light (Vis) absorption ability was recorded. The combined high effectiveness and selectivity on the NO_x abatement of the new mesocrystalline photocatalyst is reported. It is to remark that the reached maximized selectivity through the NOx process is reported by the first time and could be associated with the mesopore nature of the anatase photocatalyst.

Introduction

The arrangement of nanoparticle building blocks into well-defined assemblies and superstructures has been a crucial target in materials chemistry because these hierarchical structures lead to novel and unique properties that are not found in the individual building blocks. Those highly ordered nanoparticle superstructures in which the nanocrystals are organized in a crystallographic register are called mesocrystals, which is the abbreviation mesoscopically structured crystals [1-5].

According to Cölfen and Antonietti a mesocrystal is defined as a superstructure of crystalline nanoparticles with extended crystal faces on the scale of some hundred nanometres to micrometres [6]. However, it is interesting to point out that have been reported mesocrystalline structures made up by nanoparticle assemblies but without a well faceted external morphologies [7, 8]. The specific characteristics of mesocrystals, i. e. nanoparticle size and shape, order and porosity allow developing unusual mechanical, magnetic, chemical and optical properties. A main potential application of mesocrystals is photocatalyst due to their inner surface area and porosity, particle orientation and exposure of catalytically active crystal faces [9]. Among semiconductors advanced titania compounds have been used as photocatalysts for photodegradation of pollutants. They have not been chosen only by their chemical stability, low cost and non-toxicity but the improved photocatalytic activity of mesoporous TiO_2 consisting of compactly packed nanoparticles due to the efficient interparticle electron transfer between nanocrystals [10]. In addition, experimental and theoretical studies have suggested that the ordering of a nanocrystalline structure significantly influences charge transport and recombination [11].

Nitrogen oxides, commonly referred as NO_X - the nitric oxide (NO) and nitrogen dioxide (NO_2) -, are a group of different compounds that play a major role in atmospheric chemistry and air pollution. In spite of several procedures have been developed to reduce the NO_x emission of combustion processes, air purification in large cities and industrial areas is still a great challenge. Even though the selective catalytic or non-catalytic reduction processes are well-known, they aren´t

---

[a] Departamento de Química Inorgánica, Instituto Universitario de Investigación en Química Fina y Nanoquímica IUIQFN, Universidad de Córdoba, Campus de Rabanales, E-14071 Córdoba, Spain. E-mail: luis-sanchez@uco.es
[b] Inorganic Chemistry Department, University of Valencia, Calle Dr. Moliner 50, Burjasot (Valencia), 46100, Spain. E-mail: javier.alarcon@uv.es
[c] Chemical Engineering Department, Campus de Teatinos, Universidad de Málaga, Málaga, 29071, Spain. E-mail: marjim@uma.es

* Corresponding Authors:
Prof. Luis Sánchez
Inorganic Chemistry Department, Instituto Universitario de Investigación en Química Fina y Nanoquímica IUIQFN, Universidad de Córdoba, Campus de Rabanales, E-14071 Córdoba, Spain. E-mail: luis-sanchez@uco.es
E-mail: luis-sanchez@uco.es
Tel: +00-34-957-218634
Prof. Javier Alarcón
Inorganic Chemistry Department, University of Valencia, Calle Dr. Moliner 50, Burjasot (Valencia), 46100, Spain.
E-mail: javier.alarcon@uv.es
Tel: +00-34-96-354-4584

Electronic Supplementary Information (ESI) available: [Supplementary Information accompanying this paper includes more information about: the characterization of the samples; reported De-NO_X values of different titanium based photocatalysts; crystallographic data, chemical analysis and textural properties; X-ray diffraction; XPS spectroscopy; SEM-TEM micrographs; P25 characterization; photocatalytic activity.]. See DOI: 10.1039/x0xx00000x

View Article Online
DOI: 10.1039/C8DT00721G

applicable to directly remove the NO_X gases in the urban atmosphere (De-NO_X action), which inlets are mostly coming from the road traffic. Anatase TiO_2 has been already used mainly as integrated additive in building materials for an effective NO_x depollution in urban areas [12]. In the last few years new titania-based materials with enhanced De-NOx photocatalytic performance have been developed [13-20]. However, by those modified titania photocatalysts the NO_2 gas emissions – intermediate specie appearing during the photochemical oxidation of nitrogen oxide gases to nitrate [21] – are not fully inhibited, reaching only low levels for either a very short period of light irradiation or when negligible NO photochemical oxidation accounts (Electronic Supplementary Information (ESI), Table S1). At this point it seems to be worthwhile to remember that nitrogen dioxide (NO_2) is undesired because is 8 to 25 times more dangerous than NO. Therefore, in the De-NO_X photocatalytic process the target is not only the highest NO conversion to NO_2 but the highest conversion to nitrate or nitric acid. In our viewpoint, the selectivity of the De-NOx photocatalytic reaction, i.e. the complete transformation of NO to nitrate or nitric acid, deserves much attention and our objective is to prepare and characterize an anatase photocalyst with the suitable nanostructure, porosity and absorption of visible light to reach enhanced selectivity.

In this work, a mesocrystalline and mesoporous anatase structure is prepared by using a simple hydrothermal methodology, and characterized by several suitable techniques. As afore-mentioned the ordering of nanocrystalline structures in self-assembled nanomaterials considerably influences charge transport and recombination, which are directly related to the performance of photocatalysts. Moreover, the presence of mesoporous on these structures increases the surface area of the samples and its accessibility towards the reactant molecules, given rise to high efficiency degradation processes [22-24]. The mesocrystalline TiO_2 is studied as photocatalyst for the NO_X abatement. As a novelty, here is presented a very high selective De-NO_X titania photocatalyst combining high NO conversion values also, being both characteristics maintained for a large irradiation period. To achieve this successfully we have improved the photochemical performance of titania by expanding its activity towards Vis light and developing a mesoporous structure.

Materials and methods

Preparation of mesoporous anatase

Samples were prepared by a hydrothermal approach in two steps. The starting materials were tetraisopropyl orthotitanate ($C_{12}H_{28}O_4Ti$) and triethanolamine ($C_6H_{15}NO_3$, TEOA) as assembler agent. The nominal concentration of TiO_2 in the PTFE stainless steel autoclave was 0.25 M. The synthetic procedure can be described as follows. First, an amount of TEOA was solved in doubly distilled water to reach a titanium alkoxide/TEOA molar ratio of 1/2. This solution was hydrothermally aged in two steps. Through the first a gel was formed after heating at 100 °C for 24 h followed by the heating at 140 °C for 72 h. After the hydrothermal aging the sample was centrifuged and washed three times with water. The product was finally dried overnight in a drying oven at 100 °C and labelled as A. In order to remove TEOA, the as-prepared sample A was annealed at 350 °C for 30 min and named as A350.

Instrumentation

Chemical, structural and microstructural characteristics of nanoparticles were monitored by different experimental techniques.

Elemental analysis was carried out in a CE Instruments EA1110 Elemental Analyzer, set for the detection of Nitrogen, Carbon and Hydrogen, using atropine as standard.

X-ray diffraction (XRD) analysis (model D-8 Advance, Bruker) was performed using CuK_α radiation. The diffractometer had 1 and 3 mm divergence and antiscattering slits respectively, and a 3° 2θ range Lynxeye linear detector. For the phase identification, the diffractogram was run with a step size of 0.02 2θ° and a counting time of 0.2 s. Raman spectra of samples were obtained by means of a Raman spectrometer (Model XploRA, Horiba) with 785 nm laser. X-ray photoelectron spectra (XPS) were recorded using non-monochromated MgK radiation (hν= 1253.6 eV) and a hemi-spherical analyser operating at a constant pass energy of 29.35 eV (Physical Electronics PHI 5700 spectrometer) with the X-ray generator operating at 15 kV and 300 W.

The microstructure of samples was examined by field emission scanning electron microscopy (FESEM) at 20 kV (Model S-4800, Hitachi Ltd., Tokyo, Japan). The samples were prepared by dropping a dispersion of the powders in water directly onto the holder sample. Before the examination all specimens were coated with gold/palladium in an ion beam coater. The morphology of A and A350 titania particles was also examined using transmission electron microscopy (TEM; Model 1010, Jeol Ltd., Tokyo, Japan) at an accelerating voltage of 100 kV. Samples were dispersed in doubly distilled water and drops of the dispersion were transferred to a specimen copper grid carrying a lacey carbon film. High resolution transmission electron microscopy (HRTEM) images and selected area electron diffraction (SAED) were collected using a Tecnai G2 F20 field emission electron microscope equipped with a Gatan CCD camera. Data treatment was performed with Digital Micrograph software. The samples were prepared in a similar way to the ones for TEM.

Nitrogen absorption isotherms were obtained at 77.4 K on an ASAP 2020 instrument from Micromeritics. Specific surface areas were calculated from N_2 sorption isotherms, using the multipoint Brunauer–Emmett–Teller (BET) method and microporosity and size distributions were estimated using the t-plot, Barret-Joyner-Halenda (BJH).

UV-Vis diffuse reflectance (DR) spectra of the specimens (Model V-670, Jasco) were obtained using the diffuse reflectance technique in the range of 200 to 2500 nm.

View Article Online
DOI: 10.1039/C8DT00721G

Probe NO (>99.9%, from Abello Linde S.A.) was carried out in an IR cell connected with a conventional outgassing/gas manipulation apparatus and spectra were recorded in a Nicolet Nexus 6700 spectrometer with MCT detector.

Additional information is provided in Electronic Supplementary Information.

Photocatalysis

The photocatalytic activity of the materials towards the oxidation of NO was studied by using a 50 x 50 mm sampler holder placed in a laminar flow reactor. The reactor was placed inside a light sealed irradiation box (Solarbox 3000e RH) equipped with a Xe lamp with controlled irradiance. A 200 mg sample was used in each photocatalytic test. Artificial sunlight (25 and 550 W·m^{-2} for UV and visible irradiances, respectively) was used as irradiation. A mixture of air/NO was sent to the photoreactor. Air and NO gas streams were mixed to obtain the desired NO concentration: 500 ppb. Previously, air was conveyed by a gas-washing bottle, filled with demineralised water in order to keep the relative humidity of the supplied gas fixed at 50 ± 5 %. A flow rate, Q, of 0.75 L·min^{-1} was employed. The accurate measurement of the concentration of NO, NO_X and NO_2 was carried out using a chemiluminescence analyser (model Environnement AC32M). For each test, the air/NO gas stream ran over the sample in the dark for a period of 10 min without changes in the NO_X concentration profiles were observed, discarding the NO_X adsorption on the sample surface or its direct photolysis. Subsequently, the photoreactor was irradiated for 300 min. The tests were repeated three times to obtain average concentration values. The calculated standard deviation is ± 0.3 ppb for NO concentration and ± 1.0 ppb for NO_2 and NO_X concentration.

NO conversion, NO_2 released and NO_X conversion were defined as follows:

$$\text{NO removal rate (\%)} = \{([NO]_{in} - [NO]_{out})/[NO]_{in}\} \times 100 \qquad (1)$$

$$NO_2 \text{ released (\%)} = ([NO_2]_{out} / [NO]_{in}) \times 100 \qquad (2)$$

$$NO_X \text{ conversion (\%)} = \{([NO_X]_{in} - [NO_X]_{out})/[NO_X]_{in}\} \times 100 \qquad (3)$$

where $[NO]_{in}$, $[NO_X]_{in}$ and $[NO]_{out}$, $[NO_2]_{out}$, $[NO_X]_{out}$ denote the measured inlet and outlet concentrations, respectively, while $[NO_X] = [NO] + [NO_2]$. The used values were the average of the measured one under steady state period

Conversely, the selectivity towards the removal of efficient removal of NO_X gas molecules, *S*, here is derived according to equation (4):

$$S\,(\%) = \frac{([NOx]_{in} - [NOx]_{out})/[NOx]_{in}}{([NO]_{in} - [NO]_{out})/[NO]_{in}} \times 100 \qquad (4)$$

Results and discussion

Samples preparation and characterization

By the hydrothermal synthesis approach discrete, size-controlled and well-defined morphologically mesocrystalline nanoparticles were obtained. According to the literature different assembler [25, 26] and polymeric additives have been used [27-30]. TEOA was used as additive some years before to prepare uniform spindle-type titania by a sol-gel via [31]. The product was identified by XRD as anatase particles elongated in the direction of the c-axis, being both the size and the aspect ratio of the resulting particles dependent on the pH. The method of preparation named “the gel-sol method” was proposed for the preparation of monodisperse particles in large quantities. Polleux et al. added small amounts of low-molecular-weight functional ligands as the ethanolamine as assembler to control the assembly behaviour of preformed titania nanocrystals [26]. This synthesis was performed in benzyl alcohol as solvent. The results were not successful and the redispersions in water of surface-functionalized anatase crystals lead to uncontrolled agglomeration. In our synthetic procedure we have used titanium tetraisopropyl orthotitanate as titanium source, triethanolamine amine as assembler and water as solvent. We are going to prove that by the present synthetic procedure oriented superstructures of nanocrystals formed from crystalline building-block, although without a faceting of the nanocrystals aggregates.

The XRD pattern of the as-prepared sample after hydrothermal aging at 140 °C for 72 h, named sample A, is shown in Fig. 1(a). All detected peaks can be attributed to a crystalline phase with anatase structure (ICDD 00-021-1272). The lattice parameters of sample A obtained by refinement of the XRD pattern by the Rietveld method (Table S2) and the corresponding Rietveld plot (Fig. S1) confirmed anatase as the only crystalline phase formed through the hydrothermal aging.

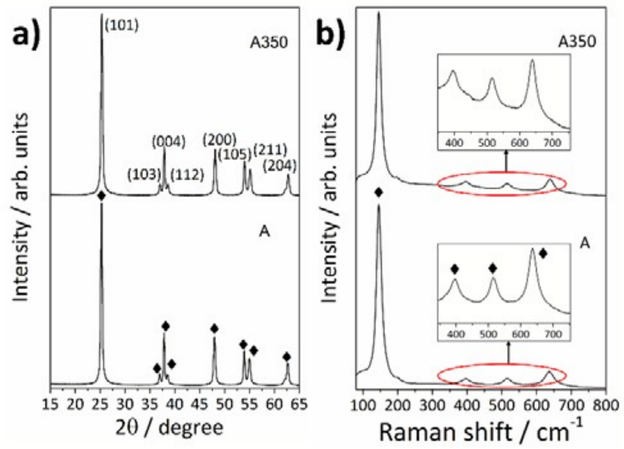

Fig. 1. (a) XRD patterns and (b) Raman spectra of samples: A (as-prepared by hydrothermal aging) and A350 (after further annealing at 350 °C for 0.5 h). [♦ = anatase phase].

The Raman spectrum of the as-prepared sample A is shown in Fig. 1b. Bands at around 142, 195, 389, 510 and 635 cm^{-1} are

View Article Online
DOI: 10.1039/C8DT00721G

detected, confirming the presence of a phase with anatase structure[32]. The amount of carbon and nitrogen determined by elemental analysis in the as-prepared sample A is shown in Table S3. The C/N ratio near to the theoretical one, 6.0, reveals the presence of TEOA attached to anatase nanoparticles, being estimated in 3.4 TEOA wt % content. Through the calcination of sample A a rapid decreases of C/N ratio and C and N content is found (Table S3). Therefore, TEOA is easily eliminated at relatively low annealing temperatures. For sample A350 (obtained after annealing the pristine sample A at 350 °C during 30 min) can be assumed that no TEOA amine remains attached to the surface so it can be considered to be pure anatase. Thus, as it could be expected for that sample A350 no structural changes were detected (Fig 1; Fig S2; Table S2).

The valence states of titanium cations were investigated by XPS measurements on the surface. Fig. S3 (left) shows comparatively the Ti 2p XPS regions of the samples A and A350. The binding energies at 458.8 eV and 464 eV are attributed to Ti^{4+} $2p_{3/2}$ and Ti $2p_{1/2}$ [33]. The XPS spectra for the O 1s region for samples A and A350 are also displayed in Fig. S3 (right). The O 1s peak can be de-convoluted in two peaks for both samples, one main peak appearing at 530 eV which is associated with lattice oxygen (Ti–O–Ti) in TiO_2 [33], being the signal at 531 eV attributed to Ti-OH hydroxyl groups [34]. No nitrogen signal was found in the region of N 1s for both samples, Fig. S4. This could be attributed to the fact that the adsorbed residual amine could have been desorbed during the overnight high vacuum treatment carried out before XPS measurement. This fact indicates that no substitutional and/or interstitial nitrogen is inside the anatase nanoparticles.

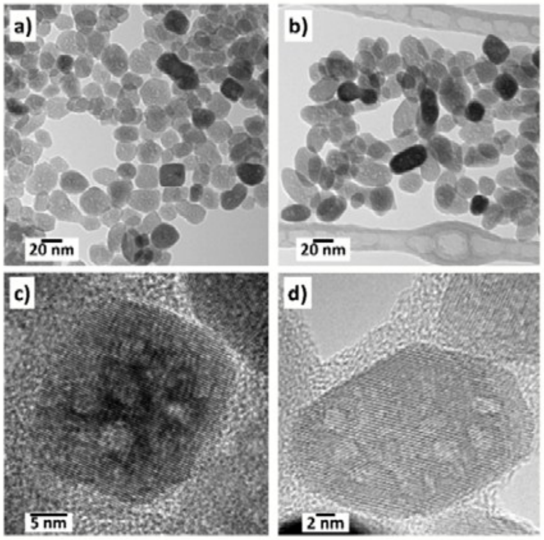

Fig. 2. TEM micrograph of samples: (a) A; (b) A350. HRTEM micrographs of samples: (c) A; (d) A350.

TEM micrographs of samples A and A350 are displayed in Figs 2a and 2b, respectively. As can be seen, both samples contain non-aggregated particles with sizes around 20 nm. It is to note that the almost spherical particles displayed in sample A become more elongated after annealing at 350 °C (sample A350). Further features related with their mesocrystallinity can also be found in the HRTEM images of these nanoparticles. Thus, the HRTEM micrographs of single particles of samples A and A350, in Figs. 2c and 2d, reveal that these particles are built from very small primary nanocrystals sized in the range 2-4 nm. Likewise, SEM micrographs of both samples A and A350 (Fig. S5) confirm the large scale-formation of particles sized around 20 nm and that the roughness of their surface indicates that both prepared anatase samples are constructed from smaller primary nanocrystals. Interestingly, the clear lattice fringes observed in HRTEM images of both single particles is in agreement with the single-crystal characteristic of them. This fact means that the resulting anatase particles A and A350 were built by aggregation of the primary anatase nanocrystals along specific directions. Anyway, it is to note that some dislocations and edge defects can be distinguished in the areas of primary nanocrystals interfaces.

HRTEM images and SAED patterns of anatase samples A and A350 shown in Fig. 3 provide further structural and microstructural features. Figs. 3a and 3d show ordered fringes with 0.35 nm of spacing in samples A and A350. Those fringes can be assigned to the (101) planes of anatase with the lattice parameters shown in Table S2. SAED of both samples, Figs. 3c and 3f, confirm the high crystallinity of the nanoparticles. All rings in the patterns can be unambiguously attributed to a crystalline phase with the structure of anatase. These results clearly indicate the formation of mesocrystalline anatase built by anatase nanocrystals sized around 2-4 nm which aggregate all oriented in the same direction giving rise to uniform assemblies (nanoparticles) with almost spherical shape.

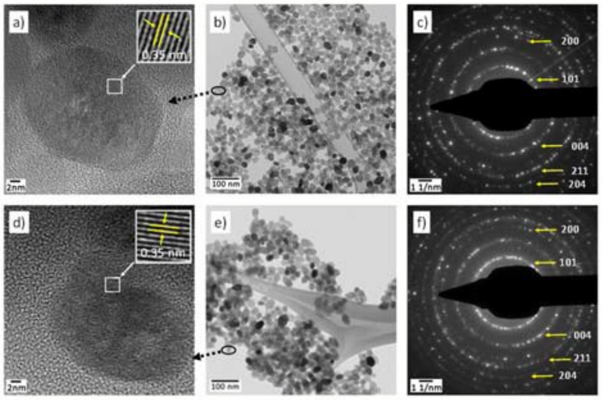

Fig. 3. HRTEM micrographs of samples A and A350: a) and d) lattice fringes of samples A and A350 associated with planes (101); b) and e) set of nanoparticles of sample A and A350; c) and f) SAED of the previous set of nanoparticles showing the indexed rings to anatase phase.

View Article Online
DOI: 10.1039/C8DT00721G

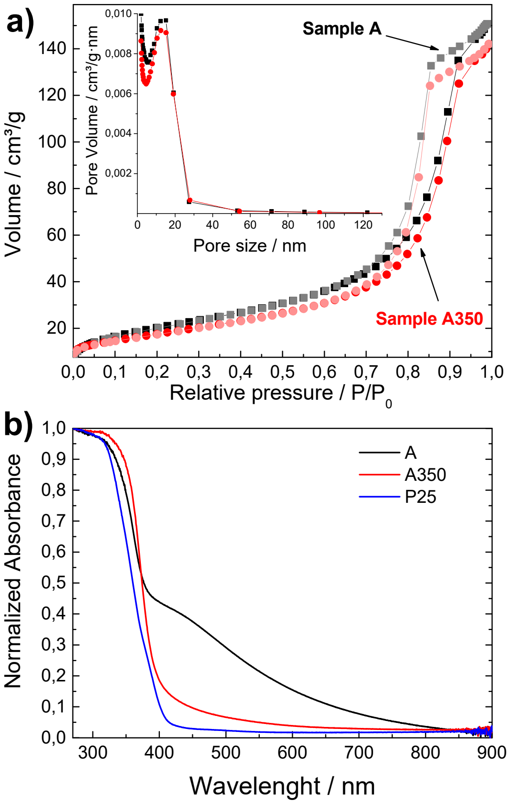

Fig. 4. (a) N_2 adsorption-desorption isotherm and (b) UV-Vis DR spectra for samples A (black) and A350 (red). The spectra of the reference P25 is also included (blue).

Owing to the well-known characteristics of titania as photocatalyst, the samples were subjected to subsequent characterization concerning to their light activation and the surface area exposed to the reactant molecules. The surface area and porous structure were elucidated from the corresponding N_2 adsorption-desorption isotherm of samples A and A350, Fig. 4a. As can be seen the isotherms of both prepared samples exhibit hysteresis loop at high relative pressure between around 0.08 and 1.0, which indicates the presence of mesopores. Table S4 summarizes the main microstructural characteristics of the prepared samples A and A350. The pore size distribution for both prepared anatase samples is similar with maximum pore size around 13 nm (Fig 4a inset), being the surface area 74.9 and 63.6 $m^2 g^{-1}$ for the samples A and A350, respectively. It is to note that the mesoporosity within these almost spherical assemblies (nanoparticles) comes from the arrangement of the primary nanocrystals. However, this porosity is not shown in HRTEM images because is disordered. The set of structural characteristics together with the results of XRD, SEM and TEM indicate that the annealing at low temperature of the as-prepared sample A has only small effects on the morphology and crystal structure (sample A350). The corresponding UV-Vis spectra of the samples are shown in Fig. 4b. As expected, a strong absorption extended over the UV radiation up to around 400 nm for the both samples. Sample A exhibits also a strong absorption on 400 – 800 nm Vis range, which could be associated with the presence of TEOA attached to the anatase nanoparticle surface [35]. Interestingly, even though the TEOA is removed, a weak absorption tail remains at wavelengths higher than 400 nm even for the sample A350. A similar behaviour was reported by Elbanna et al. [22] on preparing anatase mesocrystals, being the absorption associated to both interstitial and molecularly chemisorbed N in N-doped TiO_2 or oxygen vacancies. Since our results from XPS did not indicate the presence of structural or interstitial nitrogen it could be associated with some chemisorbed nitrogen and/or even oxygen vacancies in the lattice of mesocrystalline anatase. For comparison purposes the commercial Aeroxide® TiO_2 P25 (Evonik) was also studied, a material broadly used worldwide as reference in photocatalysis. The corresponding chemical and physical characterizations are provided in ESI, Figs. S3 and S6.

Gas-phase photocatalytic activity

The surface area values, mesopore microstructure and UV-Vis light absorption ability observed bring together the characteristics for a potential photocatalyst of high interest. In this sense, it was studied the ability of the studied samples towards the NO_X abatement through photocatalytic reactions. The De-NO_X behaviour is evaluated from the evolution of nitrogen oxides concentration profiles recorded for the mesocrystalline A350 titania sample as a function of UV-Vis irradiation time, Fig. 5a. The NO concentration only decreases under irradiation, evidencing the occurrence of a light-induced chemical reaction. Previously, during the first 10 min the gas concentration remains constant avoiding the existence of adsorption phenomena. When illumination is shutdown, the gas concentration returned almost to its initial value. The NO conversion values recorded for sample A350 were quite similar to that of reference P25 (Fig. 5b): 59 and 70 % NO conversion, respectively. In both cases, the constant values achieved after five hours indicated that a steady state condition of maximum activity was reached [36, 37]. However, the photocatalytic behaviour of sample A resulted radically different and NO concentration increases continuously under light irradiation, Fig. S7. This is consequence of the presence of TEOA molecules anchored to the surface of the titania particles, being this organic compound degraded by photocatalysis. Therefore, the pristine sample is not suitable as De-NO_X photocatalyst, being necessary to work with calcined samples on which TEOA was previously eliminated.

Anyway, the effective air quality improvement reached by photocatalyst must take into account the presence of NO_2 undesired intermediates [19, 38]. The complete photocatalytic NO_X removal from air proceeds through the complete oxidation of NO (the main nitrogen gas emitted by vehicles) to nitrate or nitric acid (NO_3^-/HNO_3). This is a complex process, that involves several intermediate species[21, 39], from which the nitrogen dioxide (NO_2) appears as highly toxic intermediate specie [40].

View Article Online
DOI: 10.1039/C8DT00721G

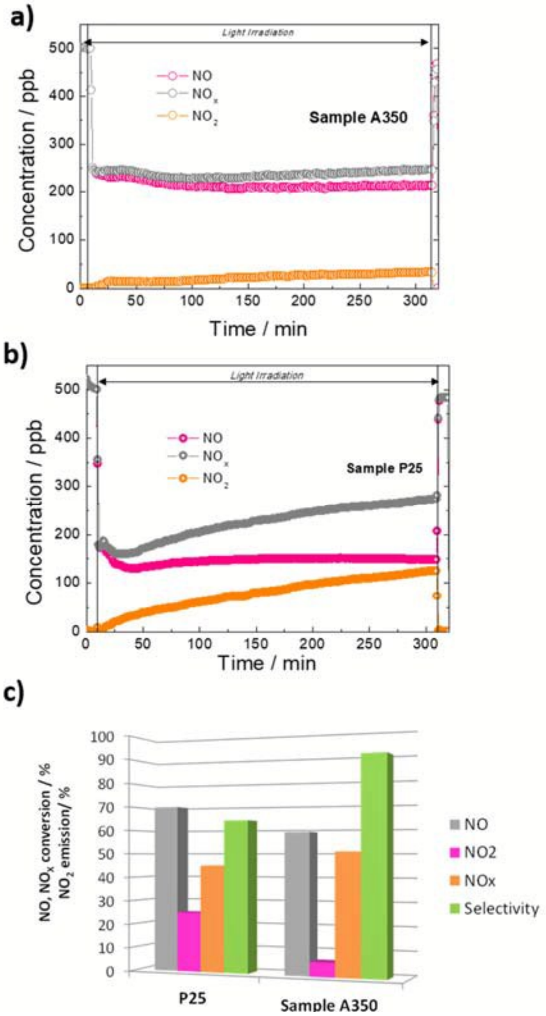

Fig. 5. Nitrogen oxides concentration profiles obtained during the photo-degradation of gaseous NO under UV-Vis irradiation on Samples (a) A350 and (b) P25. (c) NO conversion (%, grey), NO_2 released (%, pink), NO_X conversion (%, orange) and selectivity values (%, green) for A350 and P25 TiO_2 samples after five hours of light irradiation.

Therefore, the excellence for a titania De-NO_X photocatalyst won´t be only focused into obtaining the highest NO conversion values but also the highest De-NO_x selectivity. This means that no photo-oxidized NO molecules were released again to the atmosphere as NO_2. However, as it was referred in the Introduction section, it is to note that in the recent literature, the reported modified titania photocatalysts do not fully inhibit the emission of NO_2 gas. It is to remark in this sense the excellent De-NO_X activity of the A350 prepared titania. As shown in Fig. 5a, very low NO_2 concentrations were measured for sample A350. Therefore, the annealed at very low temperature titania sample A350 is able to photo-chemically oxidize the NO molecules minimizing as maximum the release of harmful nitrogen oxide gases to the atmosphere, with a very high selectivity value of 89 %. As far as we know this is the first time that this significant feature is reported for long time irradiated samples.

With regard to this, it is worth to mention that some of the samples listed on Table S1 exhibited high selectivity values (low emission of NO_2). However, it must be noted that those studies were performed at short time of irradiation (30 to 120 min), gives rise to uncertainty about those values because the NO_X removal capability of many TiO_2 based phototacalysts diminishes as the illumination proceeds in a large period [36, 37]. This feature has been related to the photochemical renoxification pathway leading to the release of NO and NO_2 from surface NO_3^- molecules [37, 41]. This is corroborated for the P25 titania, as previously reported [36]. From its NO_X concentration profiles, Fig 5b, it is observed that the theoretical full oxidation of NO towards nitrites/nitrates lowers with the irradiation time and very high amounts of NO_2 molecules are increasingly released during the experiment. In fact, after five hours of irradiation, the P25 oxidized around 70 % of molecules, but one third of them are converted in the highly toxic NO_2. Consequently, in terms of NOx removal capability the prepared titania appear as a desired photocatalyst, as summarized in Fig. 5c. Thus, it combines the high efficiency on the photochemical NO conversion (grey bar) and selectivity (green bar), resulting the highest NO_X conversion (orange bar). Moreover, the stability of sample A350 was investigated. After the photocatalytic reaction, the sample was subjected to a washing process with 5 mL of MilliQ water for 1.0 h, subsequently the product was collected by centrifugation and dried. The washed product exhibited identical chemical and physical characteristics to that of pristine sample, Figs. S8 and S9. Identical nitrogen oxides concentration profiles were recorded (Fig. S10) over the course of a new 5 hours photocatalytic cycle, supporting the excellent reusability of this catalyst in comparison with similar titania compounds [42].

It is worthwhile to note that the sample A350 also exhibits De-NO_X activity under Vis light. This functionality is of high interest for practical applications because the 4-5% of UV energy incoming from sunlight rapidly decreases to 0-2% in the cities of Central/Northern Europe or North America, owing to geography and gloomy weather condition [43]. Fig. S11 shows the NO concentration profile recorded for the A350 and P25 samples under Vis light ($\lambda > 510$ nm), obtained as a short demonstrative test. The NO conversion efficiency is proportional to the Vis absorption ability showed by each sample, Fig 4b [35]. It is outstanding that the conversion efficiency for sample A350 is 2.5 times greater than that of P25. It must be highlighted that other advanced De-NO_X titania photocatalysts and P25 also, with similar or lower particle size or higher active surface area did not shown such high selectivity (Table S1). Therefore, the singular mesopore structure seems to play an important role in the photochemical NO oxidation process inhibiting the NO_2 emission. During the photochemical oxidation of NO towards nitrites/nitrates, following the already proposed mechanisms [21], NO_2 molecules could be released to the atmosphere because: i) their weak adsorption on the TiO_2 surface [41]; ii) or the existence of a renoxification pathway involving the photochemistry of the $NO_3\bullet$ radical [44, 45].

View Article Online

DOI: 10.1039/C8DT00721G

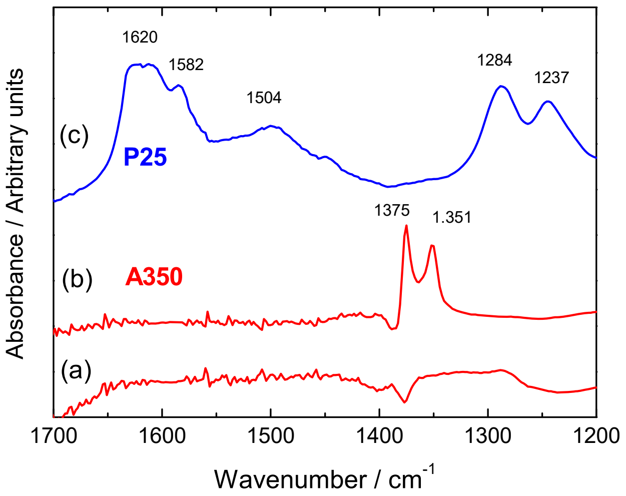

Fig. 6. (a) IR spectra of Sample A350 after 8 hours of outgassing at 50 °C in vacuum. IR spectra of samples (b) A350 and (c) P25 after exposure to 5.0 Torr NO and evacuation at 50 °C for 10 min.

In order to gain a deeper knowledge, two additional experiences were performed. Firstly, NO adsorption studies were carried out onto sample A350 surface (experimental details are provided in ESI). Prior to the NO admission into the IR cell, the sample was outgassed during 8 h at 50 °C in vacuum, Fig 6a. Subsequently, a pulse of NO (5 Torr) was introduced at the cell. The IR spectrum was recorded after gas phase evacuation at 50 °C during 10 min, Fig. 6b. For comparison, the IR spectrum for P25 sample was also obtained, Fig 6c. The spectrum of samples A350 and P25 were rather different indicating a remarkably difference for the reactive NO adsorption. For sample A350, two main IR bands located at 1.351 and 1375 cm^{-1}, characteristic of nitro/nitrite compounds (M–NO$_2$; M–ONO;) were found [46, 47]. Conversely, a set of bands at 1620, 1582, 1504, 1284 and 1237 cm^{-1} are identified on the P25 IR spectrum. According with similar experiences of NO adsorption on P25, these bands are assigned to bidentate and bridged nitrate (M–NO$_3$) [48]. The elucidation of the specific mechanism for the reactive NO adsorption in both samples is beyond to this study. However it is interesting to point out that, in contrast for sample A350, the presence of NO$_3^-$ molecules on P25 after NO adsorption let to suggest that a renoxification mechanism would be easily initiated when the surface is irradiated with UV light[44, 45], in agreement with the NO$_X$ concentration profiles of Fig 5b.

On the other hand, it is known that mesoporous networks make easy the accessibility of active reactive sites to the reactant molecules [23, 24]. These pores would be a sink on which the nitrogen oxide gases and water vapour molecules are trapped, which serve to restrain the in situ formed NO$_2$ molecules. With the aim to obtain indirect evidence about the influence of the mesoporous network onto the photochemical activity, the NOx removal capability of A600 sample (Table S2) was preliminary studied. The microstructure of this titania A600 was slightly different to that of sample A350. Even though mesopores still exist, the volume of pores and surface area are reduced more than half (Fig S12 a), this had a direct drastic influence on its photochemical activity also for a short irradiation period as shown in Fig S12 b, mainly concerning to the selectivity. The NO conversion efficiency wasn´t highly affected by the decrease of surface area. However, the loss of mesopore volume seems to be crucial because most of the NO converted molecules are now released as NO$_2$ and the selectivity value decays to 71 %. Therefore, the adsorption of NO$_2$ molecules seems to be favoured on mesostructured sample A350, facilitating the completion of the NO → NO$_2$ → NO$_3^-$ photo-oxidation process to reach the highest selective De-NO$_X$ values.

Conclusions

In summary, discrete, size-controlled and well-defined morphologically mesocrystalline anatase nanoparticles were synthesized by a hydrothermal approach. On the basis of the experimental results, it can be concluded that the as-prepared mesocrystals were constructed through assembly of nanocrystals formed in the aqueous solution at the first reaction stage. The assembler agent TEOA allowed both controlling the hydrolysis of the titanium alkoxide and stabilizing the primary anatase nanocrystals against uncontrolled aggregation. The assembler was removed by short annealing at 350 °C without significant structural and microstructural changes. The titania samples exhibited mesoporosity and photoactivity towards Vis light. Both singular characteristics allow obtaining not only high NO conversion values but also a more selective De-NO$_X$ process. The mesoporous network facilitates an almost complete NO photochemical oxidation for long irradiation periods, being this reported by the first time. The high reproducibility of this facile method of preparation of nanoparticles, it is easy scaled up to industrial level, and the high efficiency for the abatement of NO$_X$ gases provide optimism in the preparation of new advanced applications to remove the NO$_X$ breathable by the residents that are located in the polluted urban centres.

Conflicts of interest

There are no conflicts to declare.

Acknowledgements

This work was financially supported by the Spanish Government (CSD2010-00065 and TEC2014-53906-R projects), Generalitat Valenciana (Prometeo II/2015/002), Junta de Andalucía (Group FQM-175) and Córdoba University (XX PP. Modalidad 4.1). We thank to Marina Cortes Reyes for her collaboration in the NO adsorption measurements.

View Article Online
DOI: 10.1039/C8DT00721G

References

1. M. Antonietti and G. A. Ozin, *Chem. Eur. J.*, 2004, 10, 28-41.
2. M. Niederberger and H. Cölfen, *Phys. Chem. Chem. Phys.*, 2006, 8, 3271-3287.
3. L. Zhou and P. O'Brien, *Small*, 2008, 4, 1566-1574.
4. R. Q. Song and H. Cölfen, *Adv. Mater.*, 2010, 22, 1301-1330.
5. L. Zhou and P. O'Brien, *J. Phys. Chem. Lett.*, 2012, 3, 620-628.
6. H. Cölfen and M. Antonietti, *Angew. Chem. Int. Ed.*, 2005, 44, 5576-5591.
7. S. H. Lee, Y.-S. Her and E. Matijević, *J. Colloid Interface Sci.*, 1997, 186, 193-202.
8. Z. P. Zhang, H. P. Sun, X. Q. Shao, D. Li, H. Yu and M. Han, *Adv. Mater.*, 2005, 17, 42-47.
9. M. G. Ma and H. Cölfen, *Curr. Opin. Colloid Interface Sci.*, 2014, 19, 56-65.
10. N. Lakshminarasimhan, E. Bae and W. Choi, *J. Phys. Chem. C*, 2007, 111, 15244-15250.
11. Y. Zhang, J. Cai, Y. Ma and L. Qi, *Nano Research*, 2017, 10, 2610-2625.
12. R. Zouzelka and J. Rathousky, *Appl. Catal. B: Environ.*, 2017, 217, 466-476.
13. N. Todorova, T. Vaimakis, D. Petrakis, S. Hishita, N. Boukos, T. Giannakopoulou, M. Giannouri, S. Antiohos, D. Papageorgiou, E. Chaniotakis and C. Trapalis, *Catal. Today*, 2013, 209, 41-46.
14. J. Ma, H. Wu, Y. Liu and H. He, *J. Phys. Chem. C*, 2014, 118, 7434-7441.
15. N. Todorova, T. Giannakopoulou, S. Karapati, D. Petridis, T. Vaimakis and C. Trapalis, *Appl. Surf. Sci.*, 2014, 319, 113-120.
16. J. Ma, H. He and F. Liu, *Appl. Catal. B: Environ.*, 2015, 179, 21-28.
17. A. Trapalis, N. Todorova, T. Giannakopoulou, N. Boukos, T. Speliotis, D. Dimotikali and J. Yu, *Appl. Catal. B: Environ.*, 2016, 180, 637-647.
18. Y. Hu, X. Song, S. Jiang and C. Wei, *Chem. Eng. J.*, 2015, 274, 102-112.
19. J. Z. Bloh, A. Folli and D. E. Macphee, *RSC Adv.*, 2014, 4, 45726-45734.
20. A. V. Katsanaki, A. G. Kontos, T. Maggos, M. Pelaez, V. Likodimos, E. A. Pavlatou, D. D. Dionysiou and P. Falaras, *Appl. Catal. B: Environ.*, 2013, 140–141, 619-625.
21. J. Balbuena, M. Cruz-Yusta and L. Sánchez, *J. Nanosci. Nanotechnol.*, 2015, 15, 6373-6385.
22. O. Elbanna, P. Zhang, M. Fujitsuka and T. Majima, *Appl. Catal. B: Environ.*, 2016, 192, 80-87.
23. Y. Wang, H. Huang, J. Gao, G. Lu, Y. Zhao, Y. Xu and L. Jiang, *J. Mater. Chem. A*, 2014, 2, 12442-12448.
24. Y. Zhang, Z.-A. Qiao, J. Liu, X. Wang, S. Yao, T. Wang, B. Liu, Y. Ma, Y. Liu and Q. Huo, *Dalton Trans.*, 2016, 45, 265-270.
25. J. Polleux, N. Pinna, M. Antonietti and M. Niederberger, *Adv. Mater.*, 2004, 16, 436-439.
26. J. Polleux, N. Pinna, M. Antonietti, C. Hess, U. Wild, R. Schlögl and M. Niederberger, *Chem. Eur. J.*, 2005, 11, 3541-3551.
27. L. Qi, H. Cölfen, M. Antonietti, M. Li, J. D. Hopwood, A. J. Ashley and S. Mann, *Chem. Eur. J.*, 2001, 7, 3526-3532.
28. S. H. Yu, H. Cölfen and M. Antonietti, *Chem. Eur. J.*, 2002, 8, 2937-2945.
29. S. H. Yu, H. Cölfen and M. Antonietti, *Adv. Mater.*, 2003, 15, 133-136.
30. S.-H. Yu, M. Antonietti, H. Cölfen and J. Hartmann, *Nano Lett.*, 2003, 3, 379-382.
31. T. Sugimoto, K. Okada and H. Itoh, *J. Colloid Interface Sci.*, 1997, 193, 140-143.
32. W. F. Zhang, Y. L. He, M. S. Zhang, Z. Yin and Q. Chen, *J. Phys. D: Appl. Phys.*, 2000, 33, 912.
33. J. F. Moulder and J. Chastain, *Handbook of X-ray Photoelectron Spectroscopy: A Reference Book of Standard Spectra for Identification and Interpretation of XPS Data*, Physical Electronics Division, Perkin-Elmer Corporation, 1992.
34. M. E. Simonsen, Z. Li and E. G. Søgaard, *Appl. Surf. Sci.*, 2009, 255, 8054-8062.
35. A. Mills, S.-K. Lee and M. Sheridan, *Analyst*, 2005, 130, 1046-1051.
36. M. J. Hernández Rodríguez, E. Pulido Melián, O. González Díaz, J. Araña, M. Macías, A. González Orive and J. M. Doña Rodríguez, *J. Mol. Catal. A: Chem.*, 2016, 413, 56-66.
37. A. Mills and S. Elouali, *J. Photochem. Photobiol. A*, 2015, 305, 29-36.
38. Q. Zhang, Y. Huang, L. Xu, J.-j. Cao, W. Ho and S. C. Lee, *ACS Appl. Mater. Interfaces*, 2016, 8, 4165-4174.
39. A. Yamamoto, Y. Mizuno, K. Teramura, S. Hosokawa and T. Tanaka, *ACS Catalysis*, 2015, 5, 2939-2943.
40. R. J. Lewis and N. I. Sax, *Sax's Dangerous Properties of Industrial Materials*, Van Nostrand Reinhold, New York, 2012.
41. M. E. Monge, B. D'Anna and C. George, *Phys. Chem. Chem. Phys.*, 2010, 12, 8991-8998.
42. B. Tan, X. Zhang, Y. Li, H. Chen, X. Ye, Y. Wang and J. Ye, *Chem. Eur. J.*, 2017, 23, 5478-5487.
43. A. Folli, J. Z. Bloh, M. Strøm, T. Pilegaard Madsen, T. Henriksen and D. E. Macphee, *J. Phys. Chem. Lett.*, 2014, 5, 830-832.
44. O. Rosseler, M. Sleiman, V. N. Montesinos, A. Shavorskiy, V. Keller, N. Keller, M. I. Litter, H. Bluhm, M. Salmeron and H. Destaillats, *J. Phys. Chem. Lett.*, 2013, 4, 536-541.
45. R. V. Mikhaylov, A. A. Lisachenko, B. N. Shelimov, V. B. Kazansky, G. Martra and S. Coluccia, *J. Phys. Chem. C*, 2013, 117, 10345-10352.
46. K. I. Hadjiivanov, *Catal. Rev. Sci. Eng.*, 2000, 42, 71-144.
47. K. Hadjiivanov and H. Knozinger, *Phys. Chem. Chem. Phys.*, 2000, 2, 2803-2806.
48. N. Tang, Y. Liu, H. Wang and Z. Wu, *J. Phys. Chem. C*, 2011, 115, 8214-8220.